Supplementary Information

Limiting factors for charge generation in low-offset fullerene-based organic solar cells

Anna Jungbluth[1], Eunkyung Cho[2], Alberto Privitera[3], Pascal Kaienburg[1], Andreas E. Lauritzen[1], Thomas Derrien[4,], Sameer V. Kesava[1], Irfan Habib[1], Jean-Luc Brédas[2], Veaceslav Coropceanu[2], Moritz Riede[1]*

1. Department of Physics, The University of Oxford, Oxford, Oxfordshire OX13PJ, UK
2. Department of Chemistry and Biochemistry, The University of Arizona, Tucson, Arizona 85721-0088, USA
3. Department of Chemistry, University of Florence, 50019 Florence, Italy
4. Diamond Light Source, Didcot, Oxfordshire OX11 0DE, UK

* Current Address: Living Systems Institute, University of Exeter, Exeter EX4 4QD, UK

A. Microstructure Characterization

A.1 GIWAXS Scattering Results

Grazing incidence wide-angle X-ray scattering was carried out to characterize the microstructure and crystallinity of the films. **Figure S1** shows the 2D reciprocal space maps of the investigated systems. All neat films show crystalline features, in particular a strong out-of-plane peak indexed as the (200) peak, in line with previous work.[1] This indicates that the preferential orientation of the F_xZnPc molecules is with their long axes aligned roughly parallel to the out-of-plane axis direction. The peak broadening along the azimuthal angle indicates a significant spread in the orientation of crystalline domains and is seen for all neat films. At least one in-plane scattering feature attributed to the $\pi - \pi$ stacking (010) peak is also seen, along with a secondary in-plane scattering feature for neat ZnPc. The positions of the peaks are plotted in **Figure S*2***.

Increased fluorination is concomitant with increased spacing along the long axis stacking direction. F_8ZnPc and F_{16}ZnPc show a decreased $\pi - \pi$ stacking d-spacing compared to ZnPc and F_4ZnPc. The low-donor films show no crystalline features attributable to C_{60} and only faint (200) scattering features around the out-of-plane direction. The lack of scattering from C_{60}, which is the dominant molecular species in the thin films, indicates that the presence of the F_xZnPc interrupts C_{60} packing in all cases. Thus, as stated in the main text, at low concentrations all donor molecules are surrounded by acceptors and donor aggregation is largely suppressed.

Donor	100 %	5 %
ZnPc	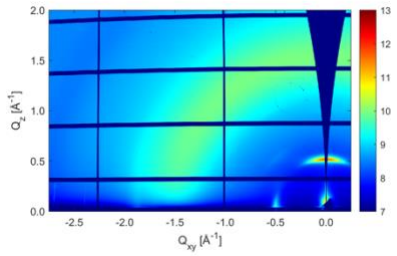	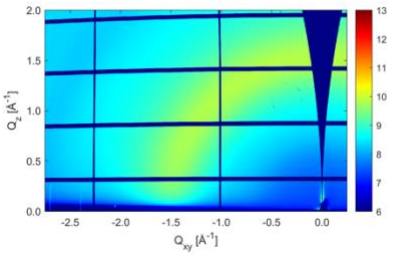
F_4ZnPc	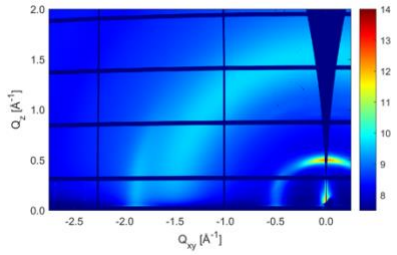	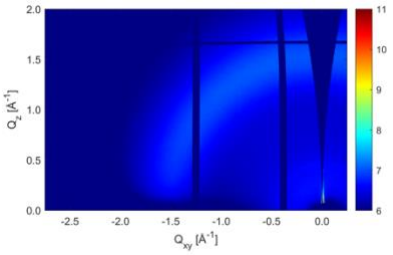
F_8ZnPc	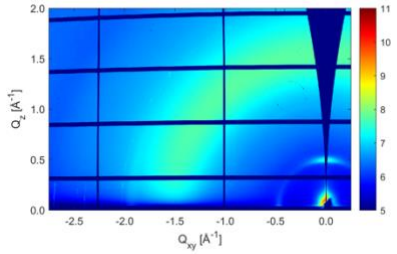	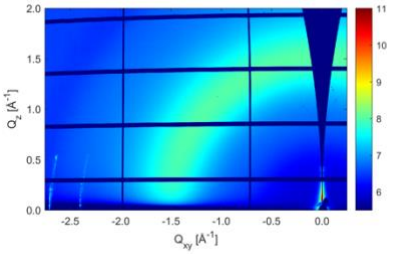
F_{16}ZnPc	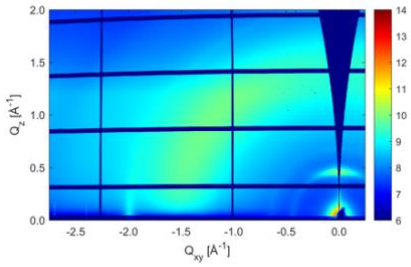	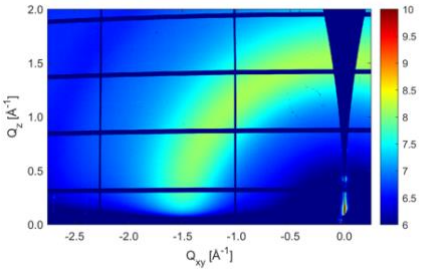

Figure S1. 2D GIWAXS reciprocal space maps of 50 nm thin film samples on quartz. The first column shows scattering of the neat F_xZnPc films, the second column shows scattering of the dilute blends. The primary out-of-plane peak is indexed as the (200) peak and the primary in-plane peak is indexed as the (010) peak.

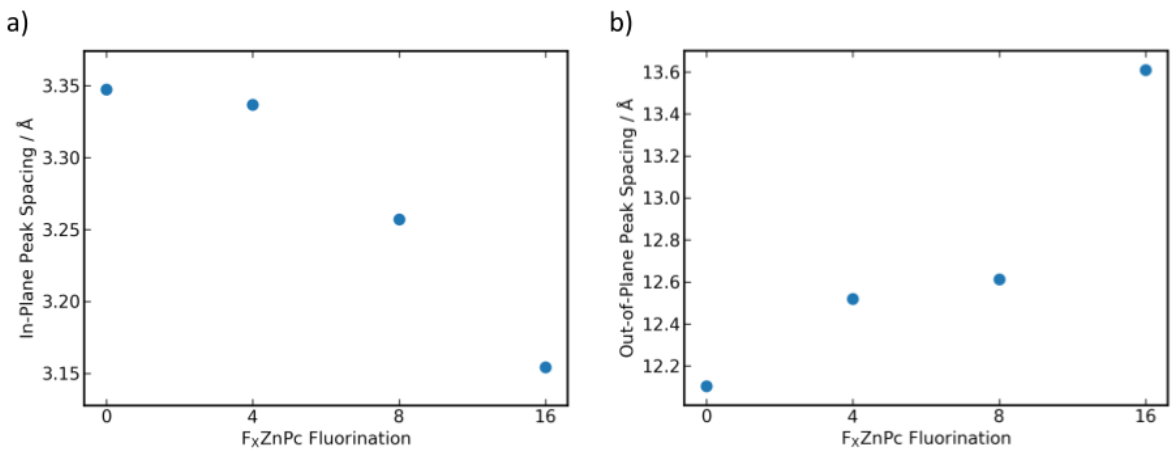

Figure S2. Real spacing of the a) in-plane (010) and b) out-of-place (200) peaks for neat F_XZnPc films on quartz.

B. Device and Thin-Film Characterization

Table S1. Device performance of dilute $F_xZnPc:C_{60}$ OSCs and neat C_{60} reference devices measured under simulated 1 Sun illumination. The mean and standard deviation of the open-circuit voltage (V_{OC}), short-circuit current (J_{SC}), and fill factor (FF) were determined for > 10 devices for all material systems, with the exact number of devices shown in the last column. The data were not mismatch corrected. However, due to the strong similarities in the absorption profile (see **Figure S5** and **Figure S6**), mismatch correction would result in similar scaling for all samples and would preserve the observed performance trends.

	V_{oc} [V]	FF [%]	J_{sc} [mAcm^{-2}]	#
$ZnPc:C_{60}$	0.78 ± 0.02	40 ± 1	3.6 ± 0.2	19
$F_4ZnPc:C_{60}$	0.89 ± 0.02	33 ± 1	3.1 ± 0.2	13
$F_8ZnPc:C_{60}$	1.14 ± 0.02	30 ± 1	1.0 ± 0.1	12
$F_{16}ZnPc:C_{60}$	1.21 ± 0.02	29 ± 1	0.8 ± 0.1	15
C_{60} Reference	1.25 ± 0.09	30 ± 1	0.9 ± 0.2	30

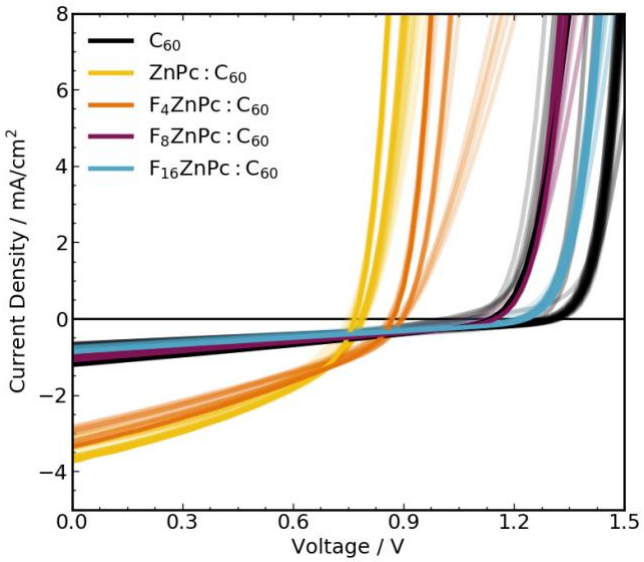

Figure S3. Current density-voltage (J – V) characteristics under simulated 1 Sun illumination for all devices fabricated for this study. The corresponding performance trends are shown in **Table S1**. The spread of measured J – V characteristics is largest for the C_{60} reference devices. This is because the neat C_{60} devices were fabricated across two years and likely encompass deviations across sample fabrication conditions (e.g., cleanliness of the evaporation chamber).

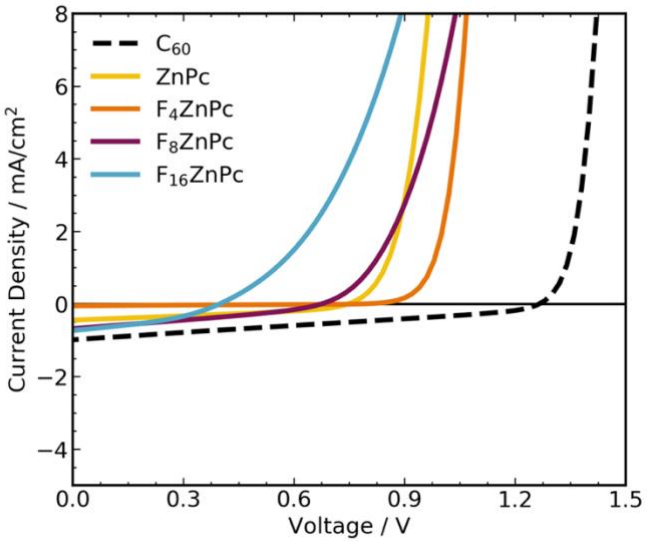

Figure S4. Current density-voltage (J – V) characteristics under simulated 1 Sun illumination for the best performing (highest V_{OC}) neat F_xZnPc OSCs.

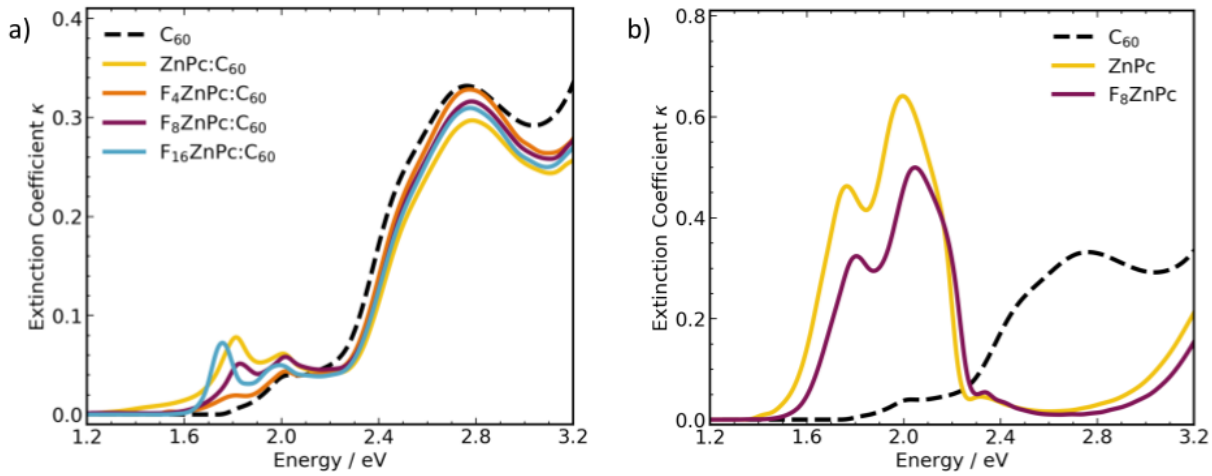

Figure S5. Extinction coefficient (κ) measured via spectroscopic ellipsometry for thin films on quartz of a) dilute $F_xZnPc:C_{60}$ and b) neat ZnPc, F_8ZnPc, and C_{60}. The absorbance of the dilute blends strongly follows that of neat $C_{60,}$ with only minor changes between 1.6 – 2.2 eV caused by the characteristic absorption doublet of F_xZnPc.[2], [3] Compared to the absorption profile of ZnPc, the slight red shift (blue shift) of the absorption peaks of F_4ZnPc and $F_{16}ZnPc$ (F_8ZnPc) is ascribed to changes in the transition dipole alignment and intermolecular coupling upon fluorination.[2]

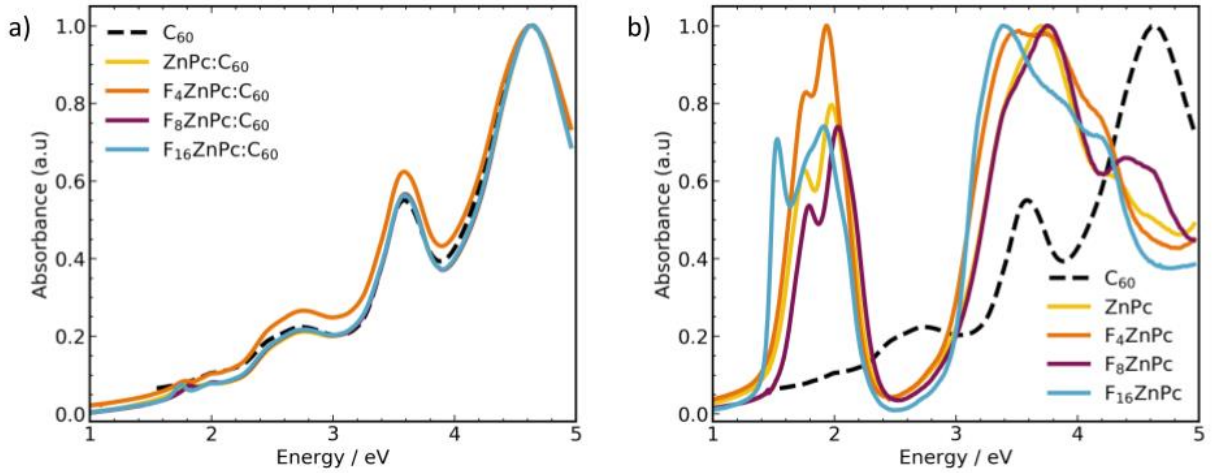

Figure S6. Normalized absorbance measured via ultraviolet-visible spectroscopy for thin film on quartz of a) dilute $F_xZnPc:C_{60}$ and b) the neat materials.

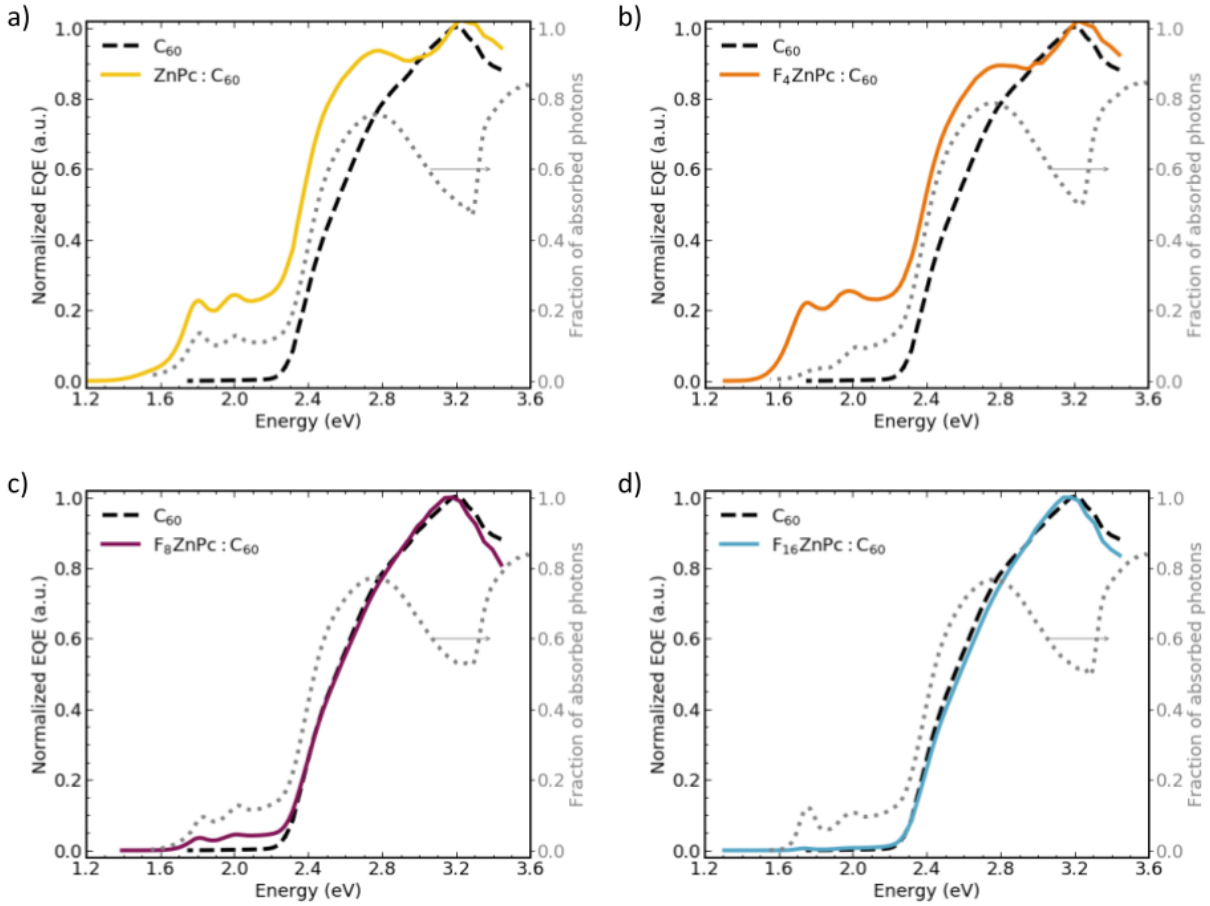

Figure S7. Comparison of photon absorption (right axis) and charge generation (left axis) for dilute donor blends of a) ZnPc, b) F_4ZnPc, c) F_8ZnPc, and d) F_{16}ZnPc and C_{60}. The complex refractive index of the blends was measured via spectroscopic ellipsometry, and the fraction of absorbed photons calculated using the transfer matrix approach.[4] This is compared to the external quantum efficiency (EQE) at room temperature of full devices with the respective blends as active layers. All material systems show photon absorption between 1.5 – 2.2 eV, but only the ZnPc and F_4ZnPc blends show efficient free charge generation in this spectral region.

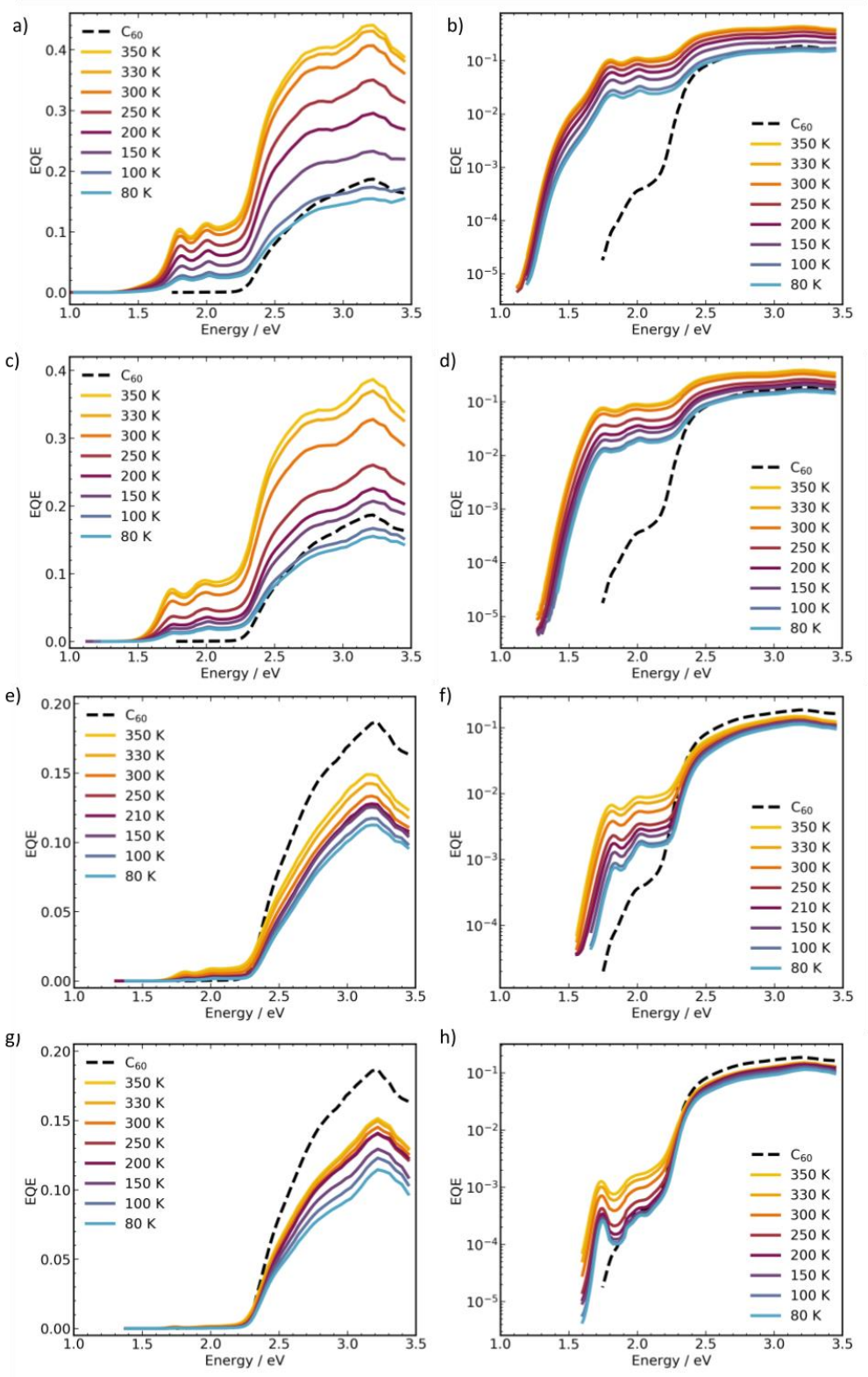

Figure S8. Temperature-dependent EQE for dilute donor blends of a) – b) ZnPc, c) – d) F_4ZnPc, e) – f) F_8ZnPc, g) – h) F_{16}ZnPc and C_{60}.

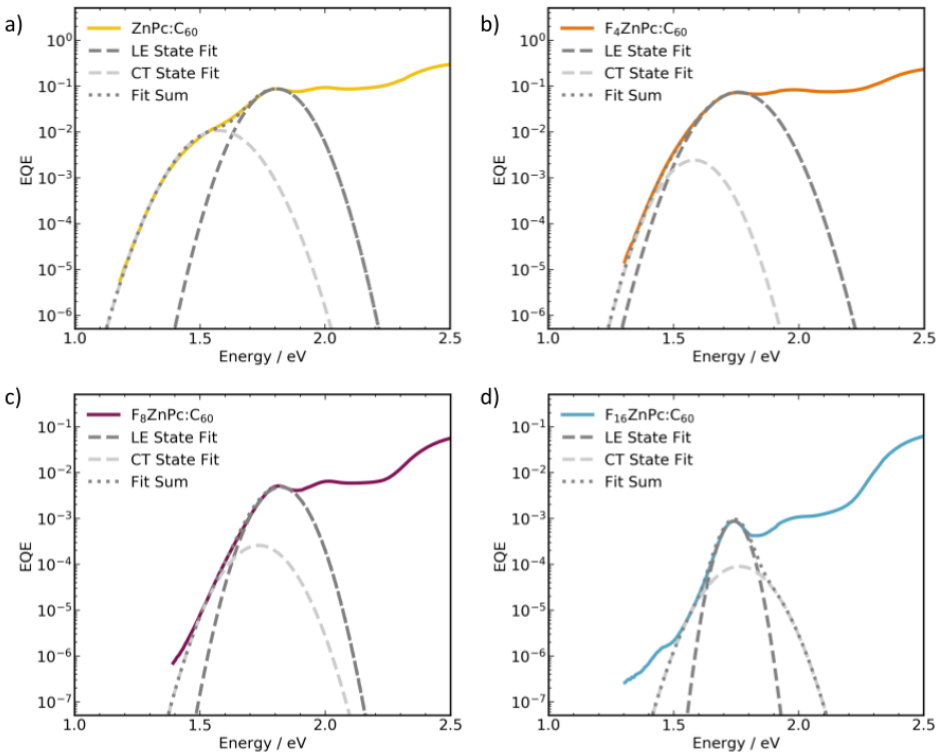

Figure S9. Fitting of room temperature EQE spectra of dilute donor blends of a) ZnPc, b) F_4ZnPc, c) F_8ZnPc, and d) F_{16}ZnPc in C_{60}. The light grey (dark grey) dashed lines show the fits of CT (local excitation (LE) singlet) states. The dotted lines indicate the sum of the fits. Both the LE and CT states were fit using the classical Marcus theory,[5], [6] and following the methodology outlined in references [7], [8].

Table S2. Results of Marcus theory fitting of local excitation (LE) singlet and CT states in the EQE of the dilute blends. The uncertainties are given as the errors on the fit, rather than deviations across samples.

	ZnPc:C_{60}	F_4ZnPc:C_{60}	F_8ZnPc:C_{60}	F_{16}ZnPc:C_{60}
E_{LE} (eV)	1.68 ± 0.01	1.59 ± 0.01	1.73 ± 0.01	1.71 ± 0.01
E_{CT} (eV)	1.38 ± 0.01	1.45 ± 0.01	1.59 ± 0.01	1.61 ± 0.01
λ_{CT} (eV)	0.199 ± 0.01	0.136 ± 0.03	0.151 ± 0.01	0.159 ± 0.01

C. Computational Details

C.1 Discussion of the DFT Results

The natural transition orbital (NTO) analysis (**Figure S11**) indicates that the lowest three excited singlet states in all complexes are CT states between the donor and acceptor. These three CT states are quasi-degenerate due to the three-fold orbital degeneracy of the C_{60} LUMO. The CT states are followed by ten quasi-degenerate C_{60} singlet states and two degenerate F_xZnPc singlet states, which are all in near resonance (**Tables S3-S6)**. For the sake of comparison, we note that measurements performed on C_{60} and ZnPc molecules embedded in matrixes of light noble gas atoms indicate that the 0-0 transition of the lowest excited singlet state has an energy of 1.94 eV and 1.91 eV for C_{60} [9] and ZnPc,[10] respectively. While the TDDFT estimates of these energies are larger than the experimental values, the TDDFT calculations correctly predict that the lowest excited states of isolated C_{60} and ZnPc molecules have comparable energies.

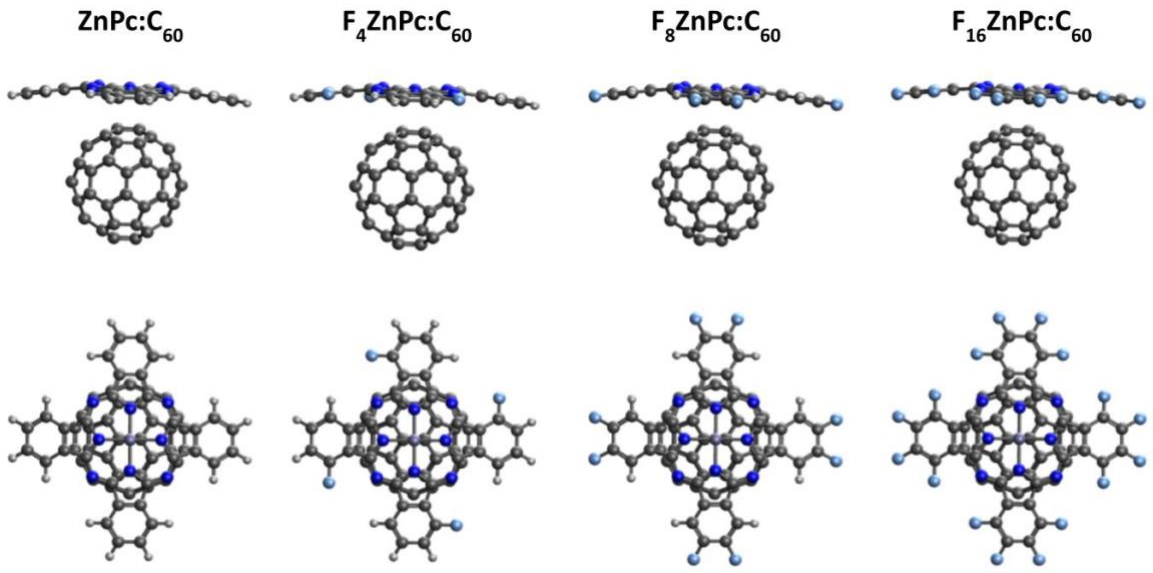

Figure S10. Optimized structures of isolated F_xZnPc:C_{60} complexes.

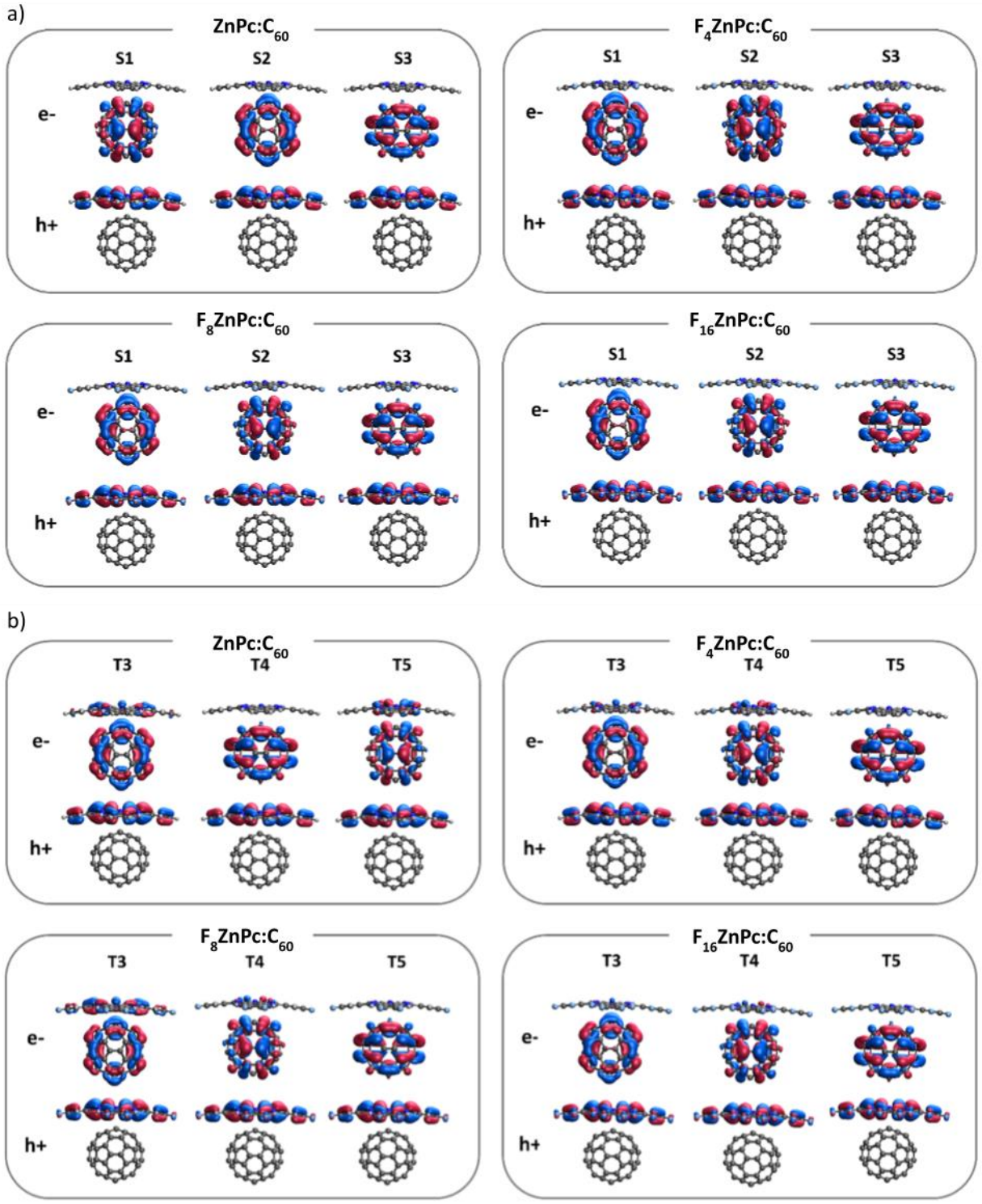

Figure S11. Electron and hole natural transition orbitals (NTOs) in the three lowest a) singlet and b) triplet CT states of the $F_xZnPc:C_{60}$ complexes when implicitly considering a dielectric medium with ε=3.

Table S3. Calculated singlet and triplet energies of the ZnPc:C_{60} complex as a function of dielectric constant; CT and LE ZnPc states are shown in red and blue, respectively.

State	[eV]	**ε=2**	**ε=3**	**ε=3.5**	**ε=4**
S1	**CT**	1.46	1.36	1.32	1.30
S2	**CT**	1.46	1.36	1.32	1.30
S3	**CT**	1.53	1.41	1.37	1.34
S4	LE-C_{60}	2.22	2.15	2.13	2.12
S5	LE-C_{60}	2.23	2.16	2.14	2.13
S6	LE-C_{60}	2.23	2.17	2.15	2.14
S7	LE-C_{60}	2.23	2.17	2.15	2.14
S8	LE-C_{60}	2.24	2.18	2.16	2.15
S9	LE-C_{60}	2.25	2.19	2.17	2.15
S10	LE-C_{60}	2.25	2.19	2.17	2.16
S11	LE-C_{60}	2.26	2.20	2.18	2.17
S12	LE-C_{60}	2.26	2.21	2.20	2.18
S13	LE-C_{60}	2.27	2.21	2.19	2.19
S14	**LE-ZnPc**	2.27	2.25	2.25	2.25
S15	**LE-ZnPc**	2.27	2.26	2.25	2.25
T1	**LE-ZnPc**	1.21	1.21	1.21	1.20
T2	**LE-ZnPc**	1.22	1.23	1.23	1.22
T3	**CT**	1.47	1.38	1.35	1.34
T4	**CT**	1.50	1.40	1.37	1.34
T5	**CT**	1.53	1.41	1.39	1.38
T6	LE-C_{60}	1.82	1.79	1.78	1.77
T7	LE-C_{60}	1.83	1.79	1.78	1.78
T8	LE-C_{60}	1.83	1.80	1.79	1.78
T9	LE-C_{60}	2.05	1.99	1.98	1.97
T10	LE-C_{60}	2.05	1.99	1.98	1.97

Table S4. Calculated singlet and triplet energies of the $F_4ZnPc:C_{60}$ complex as a function of dielectric constant; CT and LE F_4ZnPc states are shown in red and blue, respectively.

State	[eV]	**ε=2**	**ε=3**	**ε=3.5**	**ε=4**
S1	**CT**	1.50	1.39	1.36	1.34
S2	**CT**	1.50	1.39	1.36	1.34
S3	**CT**	1.57	1.45	1.41	1.39
S4	LE-C_{60}	2.21	2.16	2.14	2.12
S5	LE-C_{60}	2.22	2.16	2.14	2.13
S6	LE-C_{60}	2.22	2.17	2.15	2.14
S7	LE-C_{60}	2.23	2.17	2.15	2.14
S8	LE-C_{60}	2.23	2.18	2.16	2.15
S9	LE-C_{60}	2.23	2.19	2.17	2.16
S10	LE-C_{60}	2.25	2.19	2.17	2.16
S11	LE-C_{60}	2.25	2.20	2.18	2.17
S12	LE-C_{60}	2.25	2.21	2.19	2.18
S13	LE-C_{60}	2.26	2.21	2.19	2.18
S14	**LE-F_4ZnPc**	2.27	2.21	2.20	2.20
S15	**LE-F_4ZnPc**	2.27	2.22	2.21	2.21
T1	**LE-F_4ZnPc**	1.20	1.20	1.20	1.20
T2	**LE-F_4ZnPc**	1.20	1.21	1.21	1.21
T3	**CT**	1.50	1.41	1.38	1.36
T4	**CT**	1.54	1.44	1.41	1.38
T5	**CT**	1.57	1.44	1.42	1.40
T6	LE-C_{60}	1.83	1.79	1.78	1.77
T7	LE-C_{60}	1.83	1.79	1.78	1.78
T8	LE-C_{60}	1.83	1.80	1.79	1.78
T9	LE-C_{60}	2.05	2.00	1.98	1.97
T10	LE-C_{60}	2.05	2.00	1.98	1.97

Table S5. Calculated singlet and triplet energies of the $F_8ZnPc:C_{60}$ complex as a function of dielectric constant; CT and LE F_8ZnPc states are shown in red and blue, respectively.

State	[eV]	ε=2	ε=3	ε=3.5	ε=4
S1	**CT**	1.61	1.52	1.49	1.47
S2	**CT**	1.62	1.52	1.49	1.47
S3	**CT**	1.70	1.58	1.55	1.52
S4	LE-C_{60}	2.21	2.15	2.13	2.12
S5	LE-C_{60}	2.22	2.16	2.14	2.13
S6	LE-C_{60}	2.22	2.16	2.14	2.13
S7	LE-C_{60}	2.22	2.16	2.15	2.13
S8	LE-C_{60}	2.24	2.18	2.17	2.15
S9	LE-C_{60}	2.24	2.19	2.17	2.16
S10	LE-C_{60}	2.25	2.19	2.17	2.16
S11	LE-C_{60}	2.25	2.19	2.18	2.17
S12	LE-C_{60}	2.26	2.21	2.19	2.18
S13	LE-C_{60}	2.26	2.21	2.19	2.18
S14	**LE-F_8ZnPc**	2.27	2.27	2.27	2.27
S15	**LE-F_8ZnPc**	2.29	2.28	2.27	2.27
T1	**LE-F_8ZnPc**	1.24	1.25	1.25	1.25
T2	**LE-F_8ZnPc**	1.25	1.26	1.26	1.27
T3	**CT**	1.62	1.52	1.50	1.48
T4	**CT**	1.65	1.56	1.53	1.51
T5	**CT**	1.69	1.58	1.54	1.52
T6	LE-C_{60}	1.82	1.79	1.78	1.77
T7	LE-C_{60}	1.83	1.79	1.78	1.78
T8	LE-C_{60}	1.83	1.79	1.78	1.78
T9	LE-C_{60}	2.04	1.99	1.98	1.97
T10	LE-C_{60}	2.04	1.99	1.98	1.97

Table S6. Calculated singlet and triplet energies of the $F_{16}ZnPc:C_{60}$ complex as a function of dielectric constant; CT and LE $F_{16}ZnPc$ states are shown in red and blue, respectively.

State	[eV]	**ε=2**	**ε=3**	**ε=3.5**	**ε=4**
S1	**CT**	1.60	1.50	1.47	1.45
S2	**CT**	1.60	1.51	1.48	1.46
S3	**CT**	1.70	1.58	1.55	1.52
S4	**LE-F_{16}ZnPc**	2.16	2.14	2.13	2.12
S5	**LE-F_{16}ZnPc**	2.18	2.15	2.13	2.12
S6	LE-C_{60}	2.20	2.15	2.14	2.13
S7	LE-C_{60}	2.20	2.16	2.14	2.13
S8	LE-C_{60}	2.21	2.16	2.15	2.14
S9	LE-C_{60}	2.21	2.17	2.17	2.16
S10	LE-C_{60}	2.24	2.18	2.17	2.16
S11	LE-C_{60}	2.24	2.19	2.17	2.16
S12	LE-C_{60}	2.24	2.19	2.18	2.16
S13	LE-C_{60}	2.25	2.19	2.18	2.17
S14	LE-C_{60}	2.25	2.20	2.19	2.17
S15	LE-C_{60}	2.25	2.20	2.19	2.17
T1	**LE-F_{16}ZnPc**	1.18	1.18	1.19	1.19
T2	**LE-F_{16}ZnPc**	1.18	1.19	1.19	1.19
T3	**CT**	1.60	1.51	1.48	1.46
T4	**CT**	1.64	1.54	1.52	1.49
T5	**CT**	1.69	1.57	1.54	1.51
T6	LE-C_{60}	1.82	1.79	1.78	1.77
T7	LE-C_{60}	1.82	1.79	1.78	1.77
T8	LE-C_{60}	1.82	1.79	1.78	1.78
T9	LE-C_{60}	2.03	1.98	1.97	1.96
T10	LE-C_{60}	2.03	1.99	1.97	1.96

Table S7. Calculated energy values of the LUMO and HOMO levels for isolated F_xZnPc and C_{60} as a function of dielectric constant (ε).

	ε	ZnPc	F_4ZnPc	F_8ZnPc	$F_{16}ZnPc$	C_{60}
LUMO	2	-2.43	-2.63	-2.92	-3.25	-2.95
	3	-2.65	-2.85	-3.13	-3.45	-3.19
	3.5	-2.71	-2.91	-3.19	-3.51	-3.25
	4	-2.76	-2.95	-3.23	-3.55	-3.30
HOMO	2	-5.41	-5.54	-5.90	-6.06	-6.61
	3	-5.20	-5.34	-5.69	-5.86	-6.36
	3.5	-5.14	-5.28	-5.64	-5.80	-6.29
	4	-5.10	-5.23	-5.59	-5.76	-6.23

Table S8. Calculated transition dipole moments between the LE singlet and GS states ($\mu_{LE\text{-}GS}$), difference between the dipole moments of the CT and GS states ($\Delta\mu_{CT\text{-}GS}$), and electronic couplings between the CT and ground states ($V_{CT\text{-}GS}$), and between the CT and LE states ($V_{CT\text{-}LE}$) for the $F_xZnPc:C_{60}$ complexes as calculated via the 2-state generalized Mulliken-Hush approach based on DFT results at the LC-ωhPBE/6-31G** level of theory.

	$ZnPc:C_{60}$	$F_4ZnPc:C_{60}$	$F_8ZnPc:C_{60}$	$F_{16}ZnPc:C_{60}$
$\mu_{LE\text{-}GS}$ (D)	6.48	6.53	6.58	7.47
$\Delta\mu_{CT\text{-}GS}$ (D)	22.9	22.1	21.8	20.3
$V_{CT\text{-}GS}$ (eV)	65	75	84	101
$V_{CT\text{-}LE}$ (eV)	165	102	144	116

Table S9. Relaxation energies (λ_{rel}) of the F_xZnPc and C_{60} moelcules in the charged state and intramolecular reorganization energies for the CT state of the $F_xZnPC:C_{60}$ complex ($\lambda_{intra\text{-}CT}$), obtained from the adiabatic potential surfaces of the neutral and charged states and from a normal-mode analysis; the charged states of the F_xZnPc and C_{60} components correspond to the cation and anion states, respectively.

[meV]	Adiabatic potential surface	Normal mode
λ_{rel} (ZnPc)	21	22
λ_{rel} (F_4ZnPc)	30	31
λ_{rel} (F_8ZnPc)	37	39
λ_{rel} (F_{16}ZnPc)	51	53
λ_{rel} (C_{60})	76	75
$\lambda_{intra\text{-}CT}$ (ZnPc:C_{60})	97	97
$\lambda_{intra\text{-}CT}$ (F_4ZnPc:C_{60})	106	106
$\lambda_{intra\text{-}CT}$ (F_8ZnPc:C_{60})	113	114
$\lambda_{intra\text{-}CT}$ (F_{16}ZnPc:C_{60})	127	128

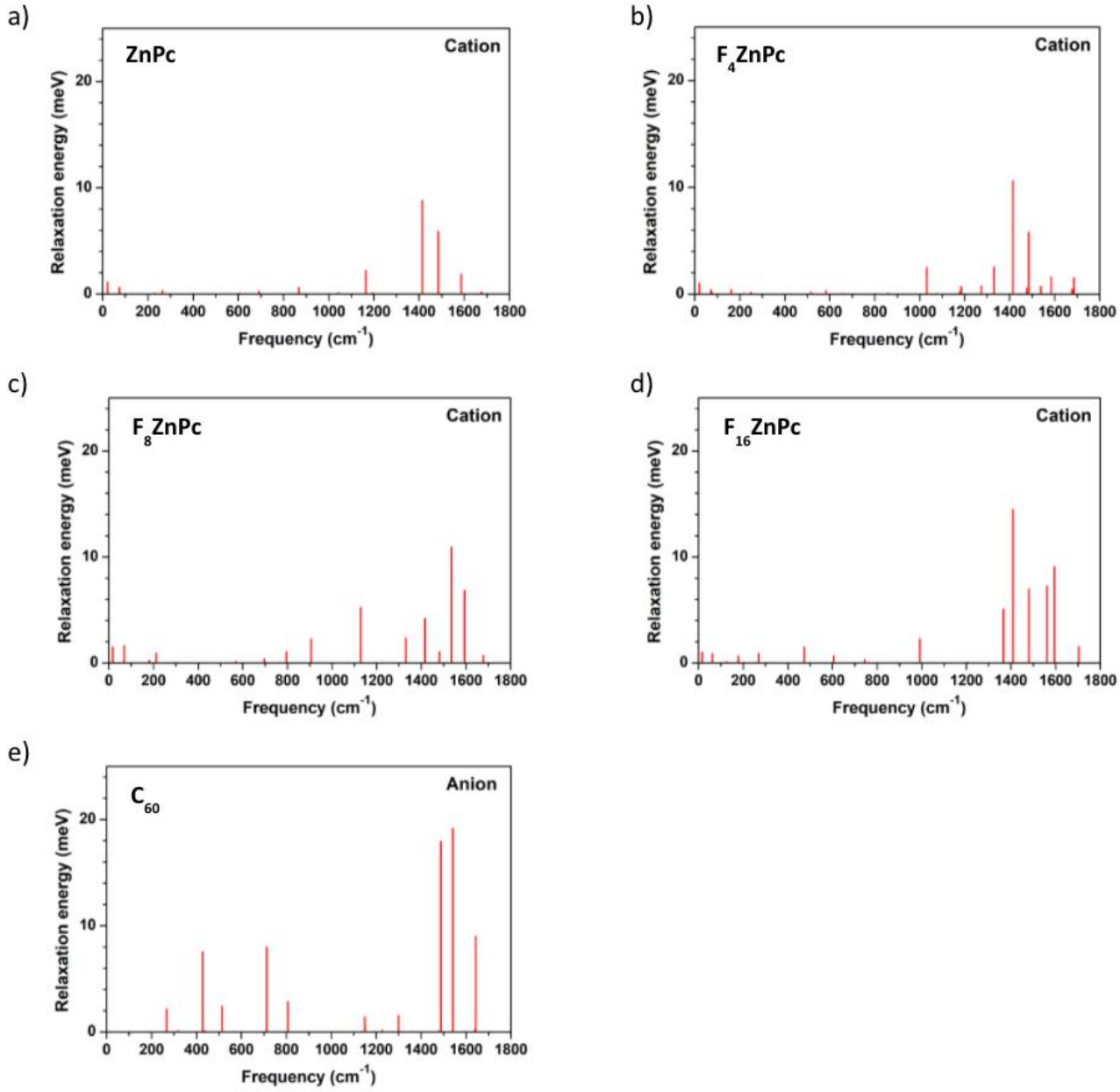

Figure S12. Decomposition of the relaxation energies of the isolated molecules into individual normal mode contributions. In all cases, the high-frequency vibrations (1400-1600 cm^{-1}) dominate.

C.2 Three-State Vibronic Model Fitting

The low-energy external quantum efficiency (EQE) spectra of the $F_xZnPc:C_{60}$ complexes were simulated by means of a three-state dynamic vibronic model we recently reported.[11] All parameters used in the three-state model study are collected in **Table S*10***.

Table S10. Parameters used in the three-state model fit of the $ZnPc:C_{60}$ and $F_4ZnPc:C_{60}$ blends: CT and LE energies (E_{CT} and E_{LE}), energy differences between LE and CT states (ΔE_{CT}), transition dipole moments to the LE states ($\mu_{LE\text{-}GS}$), state dipole moments of the CT states (μ_{CT}), electronic couplings between CT and GS states ($V_{CT\text{-}GS}$) and between CT and LE states ($V_{LE\text{-}CT}$), frequencies of low- and high-energy vibrational modes (LF and HF), and vibronic coupling constants (g) corresponding to the LE or CT state for the LF or HF vibrational mode.

	$ZnPc:C_{60}$	$F_4ZnPc:C_{60}$
E_{CT} (eV)	1.38	1.45
E_{LE} (eV)	1.69	1.65
ΔE_{CT} (eV)	0.31	0.20
$^{\#}\mu_{LE\text{-}GS}$ (D)	6.48	6.53
$^{\#}\mu_{CT}$ (D)	22.9	22.1
$^{\#}V_{CT\text{-}GS}$ (eV)	0.065	0.075
$V_{LE\text{-}CT}$ (eV)	0.090	0.081
$^{\#}$LF (cm^{-1})	100	100
$^{\#}$HF (cm^{-1})	1200	1200
g_{LF}^{LE}	2.74	2.74
g_{HF}^{LE}	0.56	0.56
g_{LF}^{CT}	4.18	5.00
g_{HF}^{CT}	0.85	1.02

$^{\#}$ These are fixed during fitting process. The others are fitted parameters.

D. EPR Measurements

D.1 EPR Analysis of neat F_xZnPc

We carried out trEPR at 80 K by using 532 nm laser excitation on the neat donor films (**Error! Reference source not found.**). All the spectra show two main species: (1) a spectrally narrow signal in neat absorption or emission at ≈345 mT, which can be attributed to photogenerated free charges and (2) a broad signal ranging from about 320 to 370 mT which can be attributed to local F_xZnPc triplet states.

The weak signal of the photogenerated charges highlights that charges are generated following laser excitation. Even without an acceptor molecule, the neat films show weak but appreciable photoactivity (**Figure S4**). The best-fit simulation values are reported in **Table S11** and discussed in the following.

A comparison of our results for the neat ZnPc film with those reported by Barbon et al. for ZnPc powder highlights a lower D value in our film.[12] Since, in first approximation, the D value is inversely proportional to the cubed delocalization r of the triplet state ($D \sim r^{-3}$), [13] a lower D value suggests that in our films the triplet exciton is slightly more delocalized. This is probably due to the defined stacking and preferential ordering of the evaporated ZnPc layer, which favors exciton delocalization.[14] A partial ordering is also suggested by the preferential ordering parameter that needs to be included in the simulation.[15]

Regarding the F_xZnPc films, their D values are larger (505-535 MHz) than for non-fluorinated ZnPc (387 MHz), which might suggest a lower delocalization of the triplet state to the nearby molecules. However, we want to emphasize that this change of D of about +33% for F_xZnPc does only correspond to a change in exciton delocalization r of approximately 10% ($1.33^{1/3}$).

Notably, the spin populations of the triplet sublevels show that in all neat donor films the triplet states are typical for intersystem crossing (ISC) triplets, as opposed to triplets populated via back electron transfer (BET). This result can be rationalized by considering that in the neat films most of the singlet excitons do not dissociate and undergo ISC before recombining to the ground state.[15], [16] Only the F_8ZnPc film shows a contribution of a geminate BET triplet in addition to ISC, which suggests that after weak charge photogeneration the charges may geminately recombine back to a low-lying triplet state in this film. This process is energetically favorable since the triplet state is lower in energy compared to the CT state (see **Table S5**). The same behavior is also observed for films of pure $PC_{60}BM$ or $PC_{70}BM$ and, while unique among the investigated F_xZnPc materials, not unusual.

D.2 Spin-polarization of BET triplets

As discussed in detail in the literature [17]–[19], geminate BET contribution can be understood in the framework of the "spin correlated radical pair (SCRP) mechanism". The standard geminate recombination pathway starts from the CT state, which in EPR spectroscopy is termed the SCRP due to the significant magnetic exchange interaction between the two unpaired spins. In fact, the radical pair is composed of a hole mainly localized on the donor and an electron mainly localized on the acceptor, that interact through the exchange interaction and generate four spin states, which for clarity we call $^1CT_0$, $^3CT_0$, $^3CT_{+1}$ and $^3CT_{-1}$. The $^1CT_0$ and $^3CT_0$ (m_s=0) spin sublevels of the SCRP are "mixed" together due to hyperfine and electron Zeeman interactions.

In this context, two distinct pathways can lead to the presence of BET triplet polarization patterns: (1) The SCRP $^3CT_0$ sublevel formed by mixing with the $^1CT_0$ undergoes a spin-allowed BET to an energetically low-lying molecular triplet T_0 state, generating an excess spin population in the

T_0. This results in a spin polarization pattern of *eaaeea* (D<0) or *aeeaae* (D>0) for the triplet exciton.[18] (2) The mixing of the $1CT_0$ and $3CT_0$ SCRP sublevels opens a spin-allowed recombination pathway for $3CT_0$ to the S_0 ground state via $1CT_0$. This process results in an excess population remaining in the $3CT_{+1}$ and $3CT_{-1}$, which undergo a spin-allowed BET to the molecular triplet T_{+1} and T_{-1} sublevels, generating an excess spin population in the T_{+1} and T_{-1}. This results in a spin polarization pattern of *eaaeea* (D>0) or *aeeaae* (D<0) for the triplet exciton.[17]

Interestingly, assuming a positive sign of D for the donor T_1 as done for similar systems in the literature, we can conclude that in our case the main polarization mechanism is the second one.[20]

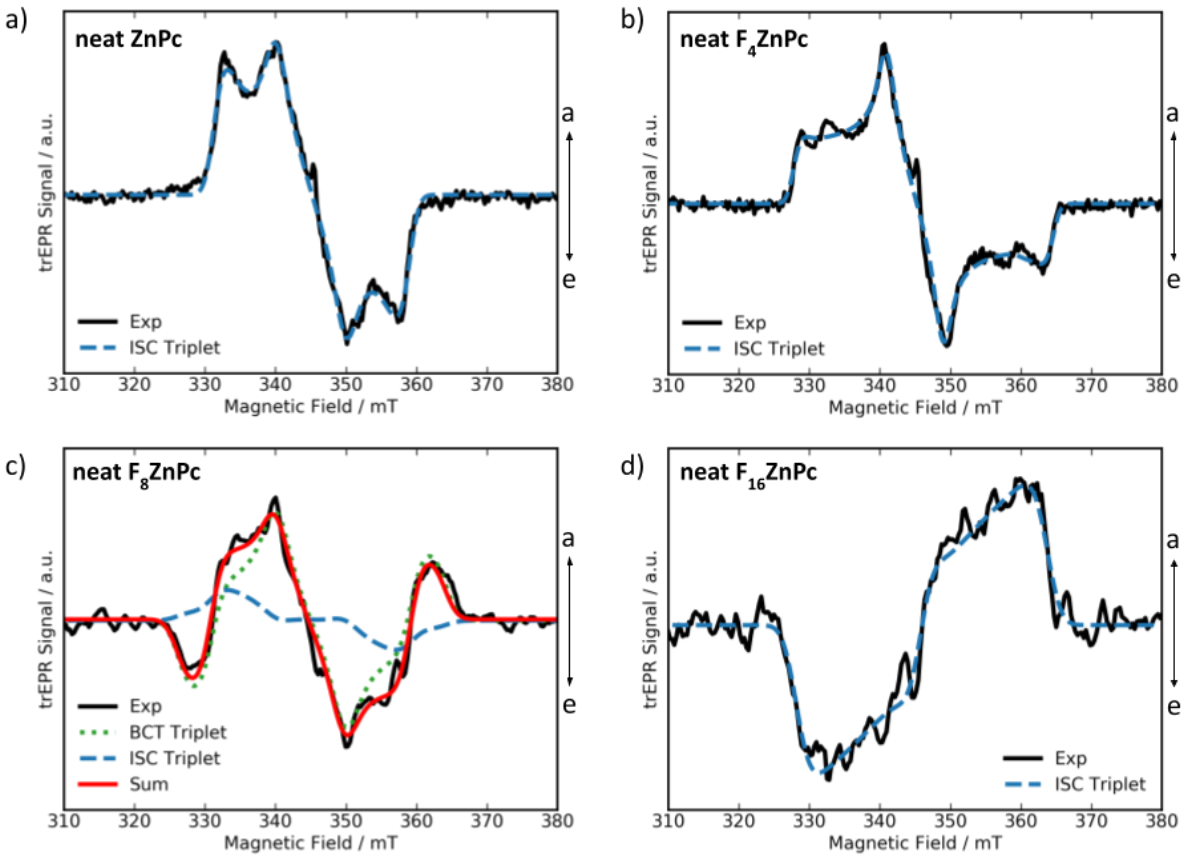

Figure S13. Time-resolved EPR spectra (black line) and best-fit simulations (red line) of neat F_xZnPc films. The trEPR spectra were recorded at 80 K after a 532 nm laser pulse (integration window 0.8-1.2 μs). Absorption (*a*) is up and emission (*e*) is down. All spectra show two main species: (1) a narrow signal in neat absorption or emission centered around 345 mT which can be attributed to photogenerated charges and (2) a broad signal ranging from about 320 to 370 mT which can be attributed to triplet states. In the case of neat ZnPc, F_4ZnPc, and F_{16}ZnPc, triplet states are populated through inter-system crossing (ISC) while neat F_8ZnPc shows both an inter-system crossing and a back electron transfer (BET) contribution. The values of the best-fit simulations are reported in **Table S11**.

Table S11. Best-fit values obtained for the trEPR spectra of neat F_xZnPc films. For each film, the populating mechanism of the triplet states and the ZFS parameters are reported. The zero-field splitting (ZFS) parameters are given in absolute value units of MHz. ISC populations order (p_1 p_2 p_3) is from low-to-high energy zero-field states. Only Lorentzian broadening was considered for both ISC and BET triplets to not over-parameterize the fitting; the linewidth is reported in units of mT. The relative weight of ISC and BET triplets is also reported. Finally, for the simulations of ISC triplets of ZnPc and F_4ZnPc, a preferential ordering contribution is needed, which suggests preferential ordering of the crystallites with respect to the substrate.

	Triplet Species	[D E] (MHz)	[p_1 p_2 p_3]	LW_{ISC} (mT)	[p_{-1} p_0 p_{+1}]	LW_{BET} (mT)	$weight_{ISC}$: $weight_{BET}$	Order
ZnPc	ISC	[387 36]	[0.48 0.19 0.33]	2.52			1:0	0.64
F_4ZnPc	ISC	[516 97]	[0.45 0.21 0.34]	1.9			1:0	0.09
F_8ZnPc	ISC+BET	[535 87]	[0.46 0.47 0.07]	3.4	[1 0 1]	3.2	0.22:0.78	
F_{16}ZnPc	ISC	[505 150]	[0.25 0.39 0.36]	3.5			1:0	

References

[1] T. L. Derrien, A. E. Lauritzen, P. Kaienburg, E. Hancox, C. Nicklin, and M. Riede, "Interfacial rearrangements and strain evolution in the thin film growth of ZnPc on glass," *Phys Rev Mater*, vol. 6, no. 3, p. 033401, Mar. 2022, doi: 10.1103/PhysRevMaterials.6.033401.

[2] M. Brendel *et al.*, "The effect of gradual fluorination on the properties of FnZnPc thin films and FnZnPc/C60 bilayer photovoltaic cells," *Adv Funct Mater*, vol. 25, no. 10, pp. 1565–1573, Mar. 2015, doi: 10.1002/adfm.201404434.

[3] H. Brinkmann *et al.*, "Fluorinated phthalocyanines as molecular semiconductor thin films," *Physica Status Solidi (A) Applications and Materials Science*, vol. 205, no. 3, pp. 409–420, Mar. 2008, doi: 10.1002/pssa.200723391.

[4] G. F. Burkhard, E. T. Hoke, and M. D. McGehee, "Accounting for interference, scattering, and electrode absorption to make accurate internal quantum efficiency measurements in organic and other thin solar cells," *Advanced Materials*, vol. 22, no. 30, pp. 3293–3297, Aug. 2010, doi: 10.1002/adma.201000883.

[5] K. Vandewal, K. Tvingstedt, A. Gadisa, O. Inganäs, and J. v. Manca, "On the origin of the open-circuit voltage of polymer-fullerene solar cells," *Nat Mater*, vol. 8, no. 11, pp. 904–909, 2009, doi: 10.1038/nmat2548.

[6] K. Vandewal, K. Tvingstedt, A. Gadisa, O. Inganäs, and J. v. Manca, "Relating the open-circuit voltage to interface molecular properties of donor:acceptor bulk heterojunction solar cells," *Phys Rev B Condens Matter Mater Phys*, 2010, doi: 10.1103/PhysRevB.81.125204.

[7] A. Jungbluth, P. Kaienburg, and M. Riede, "Charge transfer state characterization and voltage losses of organic solar cells," *Journal of Physics: Materials*, vol. 5, no. 2, p. 024002, Apr. 2022, doi: 10.1088/2515-7639/ac44d9.

[8] T. Y. Li *et al.*, "Boron dipyrromethene (BODIPY) with: Meso -perfluorinated alkyl substituents as near infrared donors in organic solar cells," *J Mater Chem A Mater*, vol. 6, no. 38, pp. 18583–18591, 2018, doi: 10.1039/c8ta06261g.

[9] G. Orlandi and F. Negri, "Electronic states and transitions in C60 and C70 fullerenes," *Photochemical and Photobiological Sciences*, vol. 1, no. 5, pp. 289–308, May 2002, doi: 10.1039/b200178k.

[10] T. C. Vancott *et al.*, "Magnetic Circular Dichroism and Absorption Spectrum of Zinc Phthalocyanine in an Argon Matrix between 14 700 and 74 000 cm"1," 1989. [Online]. Available: https://pubs.acs.org/sharingguidelines

[11] X. K. Chen, V. Coropceanu, and J. L. Brédas, "Assessing the nature of the charge-transfer electronic states in organic solar cells," *Nat Commun*, vol. 9, no. 1, Dec. 2018, doi: 10.1038/s41467-018-07707-8.

[12] A. Barbon, M. Brustolon, and E. E. van Faassen, "Photoexcited spin triplet states in zinc phthalocyanine studied by transient EPR," *Physical Chemistry Chemical Physics*, vol. 3, no. 23, pp. 5342–5347, 2001, doi: 10.1039/b106169k.

[13] S. Richert, C. E. Tait, and C. R. Timmel, "Delocalisation of photoexcited triplet states probed by transient EPR and hyperfine spectroscopy," *Journal of Magnetic Resonance*, vol. 280, pp. 103–116, Jul. 2017, doi: 10.1016/j.jmr.2017.01.005.

[14] A. Privitera *et al.*, "Electron spin as fingerprint for charge generation and transport in doped organic semiconductors," *J Mater Chem C Mater*, vol. 9, no. 8, pp. 2944–2954, Feb. 2021, doi: 10.1039/d0tc06097f.

[15] T. Biskup, “Structure-function relationship of organic semiconductors: Detailed insights from time-resolved EPR spectroscopy,” *Front Chem*, vol. 7, no. FEB, 2019, doi: 10.3389/fchem.2019.00010.
[16] A. J. Gillett *et al.*, “The role of charge recombination to triplet excitons in organic solar cells,” *Nature*, vol. 597, no. 7878, pp. 666–671, Sep. 2021, doi: 10.1038/s41586-021-03840-5.
[17] L. Franco *et al.*, “Time-resolved EPR of photoinduced excited states in a semiconducting polymer/PCBM blend,” *Journal of Physical Chemistry C*, vol. 117, no. 4, pp. 1554–1560, Jan. 2013, doi: 10.1021/jp306278v.
[18] S. A. J. Thomson, J. Niklas, K. L. Mardis, C. Mallares, I. D. W. Samuel, and O. G. Poluektov, “Charge Separation and Triplet Exciton Formation Pathways in Small-Molecule Solar Cells as Studied by Time-Resolved EPR Spectroscopy,” *Journal of Physical Chemistry C*, vol. 121, no. 41, pp. 22707–22719, Oct. 2017, doi: 10.1021/acs.jpcc.7b08217.
[19] C. D. Buckley, D. A. Hunter, P. J. Hore ’, and K. A. Mclauchlan, “Electron Spin Resonance of Spin-Correlated Radical Pairs,” 1987.
[20] T. Ikoma, K. Akiyama, S. Tero-Kubota, and Y. Ikegami, “Time-Resolved ESR Studies on the Excited Triplet States and Photoenolization of 2-Methylacetophenone and Related Molecules,” 1989. [Online]. Available: https://pubs.acs.org/sharingguidelines